Connecting shear flow and vortex array instabilities in annular atomic superfluids

D. Hernández-Rajkov [1,2] ✉, N. Grani[1,2,3], F. Scazza [1,2,4], G. Del Pace [1,3], W. J. Kwon [5], M. Inguscio[1,2,6], K. Xhani [2], C. Fort [1,2,3], M. Modugno [7,8,9], F. Marino [2,10] & G. Roati[1,2]

At the interface between two fluid layers in relative motion, infinitesimal fluctuations can be exponentially amplified, inducing vorticity and the breakdown of laminar flow. While shear flow instabilities in classical fluids have been extensively observed in various contexts, controlled experiments in the presence of quantized circulation are quite rare. Here we observe how the contact interface between two counter-rotating atomic superflows develops into an ordered circular array of quantized vortices, which loses stability and rolls up into vortex clusters. We extract the instability growth rates and find that they obey the same scaling relations across different superfluid regimes, ranging from weakly interacting bosonic to strongly correlated fermionic pair condensates. Our results establish connections between vortex arrays and shear flow instabilities, suggesting a possible interpretation of the observed quantized vortex dynamics as a manifestation of the underlying unstable flow. Moreover, they open the way for exploring out-of-equilibrium phenomena such as vortex matter phase transitions and the spontaneous emergence and decay of two-dimensional quantum turbulence.

A close relationship exists between vortices and shear flow instabilities in fluid mechanics. In classical hydrodynamics, the interface between two fluid layers in relative motion is identified by an ideal surface containing an infinite number of line vortices, namely a vortex sheet[1]. More than one century ago, Lord Kelvin and von Helmholtz predicted the dynamical instability of such a vortex sheet[2,3], later generalized by Rayleigh to the case of a finite-width shear layer[4,5]. The Kelvin–Helmholtz instability (KHI) initially manifests itself as a wave-like deformation of the interface, exponentially growing in time with a rate proportional to the relative velocity between the two fluids. It quickly leads to the twisting of the vortex sheet[1,5] and eventually to a turbulent mixing of spiralling structures[6–9]. Starting from the seminal experiments by Reynolds in 1883 (ref. 10), the KHI has been the subject of extensive research and experimentation[11–13].

The past few decades have seen exciting advances in the field of superfluidity—in particular, in ultracold atomic systems[14]—owing to an ever-increasing capability to manipulate pristine quantum systems in which vorticity is quantized, and dissipation occurs through channels different from those in ordinary fluids. A natural question is whether these key differences affect the onset and the microscopic nature of flow instabilities and to what extent classical scaling relations apply to superfluids, particularly in the presence of strong interactions. Theoretical investigations in quantum fluids have been mostly focused on the stability of the interface between distinct sliding fluid components,
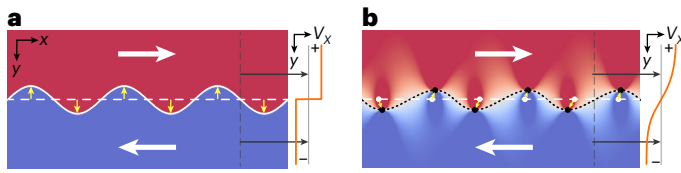
Fig. 1 | Instability of classical and quantum counter-propagating shear flows. a, The (zero-width) vortex sheet separating two counter-propagating classical flows at time $t = 0$ (horizontal dashed line) is unstable due to the KHI, developing at $t > 0$ a wave-like deformation (solid line) with characteristic wave vectors that grow exponentially in time. **b**, In single-component superfluids, a shear-flow instability manifests itself as the deformation of the discrete vortex sheet[24,25] formed by an array of quantized vortices (dots). Except at the position of the vortices, the tangential velocity gradually changes from the bulk value of one region to that of the other, giving rise to an effective finite-width shear layer. Similarly to a real interface separating different sliding fluids, this layer (dotted line) is unstable and breaks down as evidenced by the vortex motion[26,27]. In **a** and **b**, background colours display the magnitude of the velocity component tangential to the initial shear layer. Vertical cuts of the tangential velocity profiles along the transverse direction are also depicted on the right of each panel (orange lines).

such as superfluid and normal phases of the same liquid[15,16], and in binary Bose–Einstein condensates[17–20] (BECs). Experimental observations are limited to the interface between the A and B phases of ^{3}He in a rotating cryostat[21,22]. More recently, the appearance of streets of quantized vortices in rapidly rotating atomic BECs has been associated with Kelvin–Helmholtz dynamics[23].

In general, the only necessary condition for the onset of an instability is a shear flow[1], that is, two adjacent layers flowing at different velocities within a single homogeneous fluid (Fig. 1a). In this Article, we describe the realization of such a minimal scenario by engineering two counter-propagating flows in a single-component atomic superfluid. Recently, this approach has been proposed as a possible route to KHI in quantum fluids and numerically validated for atomic BECs[24,25]. Owing to the continuity of the wavefunction and the quantization of circulation, superfluids cannot support a continuous vortex sheet. Instead, a regular array of quantized vortices forms along the shear layer[24,25] acting as a discrete version of a vortex sheet (Fig. 1b). The vortex array is unstable, and its dynamics can be directly mapped onto the instability of the associated counter-propagating flows, establishing a direct relationship between shear flow and vortex rows instabilities[26,27]. In our experiment, we create a circular shear layer by exciting two counter-rotating superflows in a ring-shaped geometry. We observe the formation of a periodic, circular array of quantized vortices—a vortex 'necklace'—that rapidly breaks down, with nearby vortices rolling up and eventually displaying complex correlated trajectories. We demonstrate that the departure from the circular vortex necklace proceeds according to characteristic rates described by universal scaling relations across all the different superfluid regimes. Interestingly, the measured scalings are compatible with the classical KHI of a finite-width shear layer. Our observations establish atomic Fermi superfluids as a versatile laboratory for quantum fluid dynamics experiments. We overcome typical difficulties that affect experiments with helium quantum fluids[21,22], especially in terms of single-vortex detection and reconstruction of vortex trajectories[28].

Our experiment starts with two thin and uniform Fermi superfluids comprising $N_p \approx 3 \times 10^4$ pairs of fermionic ^{6}Li atoms (Methods). Interactions between atoms forming the pairs are encoded in the s-wave scattering length a. This can be tuned through a broad Feshbach resonance, entering different superfluid regimes ranging from weakly interacting BECs of tightly bound molecules ($1/k_F a > 1$) to strongly correlated unitary Fermi gases (UFG, $1/k_F a \approx 0$) and Bardeen–Cooper–Schrieffer (BCS, $1/k_F a < 0$) superfluids. Here, $k_F = (M E_F/\hbar^2)^{1/2}$ is the Fermi wavevec-

tor, estimated from the system global Fermi energy E_F, and M is the mass of a fermion pair. The superfluids are confined in two concentric annular optical traps initially separated by a narrow potential barrier, resulting in two reservoirs with equal density $n_{2D} = 4.96(2)$ μm^{-2} (Fig. 2a). Sample temperatures are well below the critical temperature T_c of the superfluid transition, $T = 0.3(1)T_c$, corresponding to near-unity superfluid fractions in all interaction regimes. The superfluid healing length ξ is always smaller than the vertical cloud size, making the superfluid dynamics three-dimensional. In contrast, vortex dynamics remain two-dimensional (2D) since only a few Kelvin modes of vortex lines are accessible (Methods).

We excite persistent flows in each reservoir by optically imprinting a dynamical phase onto the superfluid rings[29]. In particular, we drive independent currents by shining oppositely oriented, azimuthal light gradients onto the internal and external rings (Methods). With this procedure, we set integer quantized circulations $w_{i,e}$ with corresponding velocity fields $v_{i,e}(r) = \hbar w_{i,e}/(Mr)$, where r is the distance from the centre, and the indices 'i' and 'e' refer to the internal and external rings, respectively. The relative velocity at the interface equals $\Delta v = \hbar(w_e - w_i)/(MR_0)$, where R_0 is the radius of the circular potential barrier separating the reservoirs. In all interaction regimes, we fix $w_e = -w_i$ and only consider velocities $\Delta v_{max} < 0.7 c_s$, where c_s is the measured speed of sound in the bulk (Supplementary Information).

We merge the two counter-rotating superfluids by gradually lowering the barrier potential. To follow the evolution of the flow, we image the atomic density profile after a short time-of-flight (TOF) expansion at varying times during the barrier removal. As shown in Fig. 2b, as long as the barrier separates the two superfluid rings, a spiral interference pattern is observed due to the presence of an azimuthal phase gradient between the rings. The number of spiral arms matches the number $\Delta w \equiv |w_e - w_i|$ of 2π phase slips at the circular interface[29–31]. Eventually, when the barrier is completely removed, and the two superfluids come into full contact ($t = 0$), we observe a necklace of $N_v \approx \Delta w$ singly charged, quantized vortices[24,25] with the same circulation sign determined by vorticity (Methods). Soon after the vortex necklace emerges, its periodicity breaks down, and vortices start pairing up in a quasi-synchronous process. As time progresses, metastable clusters of increasingly larger size form, following trajectories reminiscent of the characteristic Kelvin–Helmholtz roll-up dynamics[32] (Fig. 2c–f).

We reconstruct the evolution of the vortex necklace by characterizing it through the vortex structure factor[33]. In our circular geometry, although vortices move both in radial and azimuthal directions (Fig. 2c), the vortex array deformations can be efficiently characterized by the angular structure factor, defined as $S(m,t) = (1/N_v) \sum_{j,l} \exp[im(\theta_j(t) - \theta_l(t))]$. Here, $\theta_j(t)$ is the angular position of the jth vortex and m is the integer winding number of the mode, defined as $m = kR_0$, where k is the mode wavenumber. Figure 3a displays the average $s(m,t) = S(m,t)/N_v$ measured for $1/k_F a = 0.0(1)$ and $\Delta w = 12$. The spectral peak at $m = \Delta w$, characteristic of a periodic necklace with Δw equally spaced vortices, evolves towards lower angular modes while simultaneously broadening. Similar behaviour is found in all interaction regimes. The increasing population of lower modes identifies the breakdown of the necklace structure. For most modes m, we observe that $s(m,t)$ grows exponentially in time as $s(m,t) \sim e^{2\sigma_m t}$, where σ_m is the growth rate of the mth mode. As an example, Fig. 3b presents the behaviour for $m = 6$.

We analyse the spectral dependence of σ_m for different relative velocities using the point vortex model (PVM) (Supplementary Information). This model treats each vortex as a point particle advected by the velocity field generated by all other vortices. The vortex motion is thus determined by the background flow, which, in turn, emerges as a phenomenon associated with the vortex dynamics. As discussed in refs. 26,27, the instability appears as the departure from the initial ordered vortex configuration with characteristic rates given by
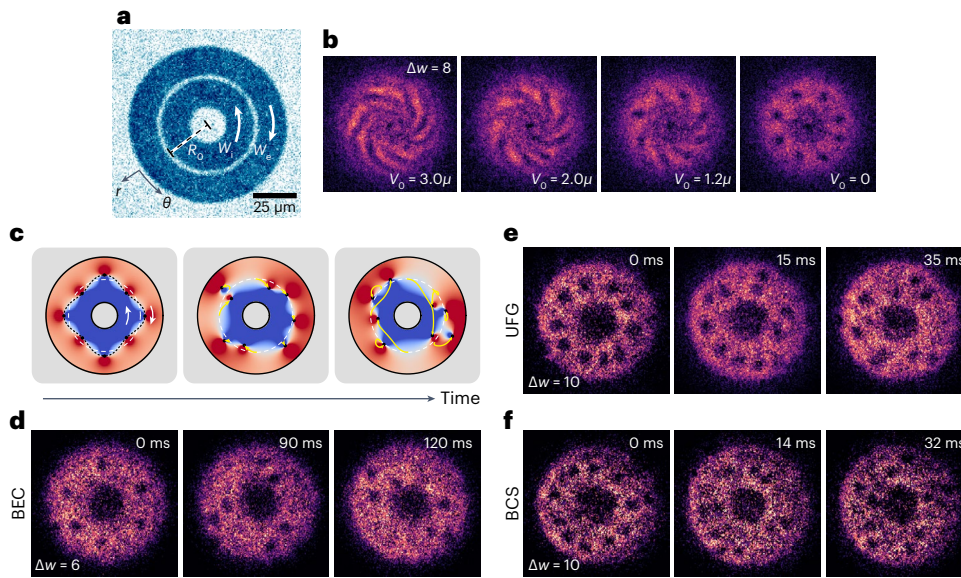
Fig. 2 | Shear flow preparation and emerging vortex dynamics. a, The in situ density profile of two concentric counter-rotating superfluids set in relative motion by a phase-imprinting technique while being separated by a potential barrier with full width at half maximum of 1.4(1) μm. **b**, Single-shot TOF images in the BEC regime for $\Delta w = 8$, as the barrier height V_0 is gradually lowered from $V_0 \approx 3.5\mu$ to 0, where μ is the superfluid chemical potential (Supplementary Information). A necklace of $N_v = 8$ vortices spontaneously forms at the location of the shear layer. **c**, PVM simulations of the dynamics of a necklace with $N_v = 8$ vortices. In the left panel, the dotted sinusoidal line illustrates the interface mode

$m = 4$. Vortex trajectories are indicated by the curved yellow arrows, while the background colours refer to the magnitude of the tangential component of the velocity, with the flow directions specified by white arrows. **d–f**, Typical single-shot TOF images of the vortex patterns obtained at different times $t \geq 0$ after merging the two superfluids in distinct interaction regimes: BEC at $1/k_F a = 4.3(1)$ with $\Delta w = 6$ (**d**), UFG at $1/k_F a = 0.0(1)$ with $\Delta w = 10$ (**e**) and BCS superfluid at $1/k_F a = -0.3(1)$ with $\Delta w = 10$ (**f**). In all interaction regimes, the vortex necklace destabilizes for $t > 0$ and few vortex clusters form.
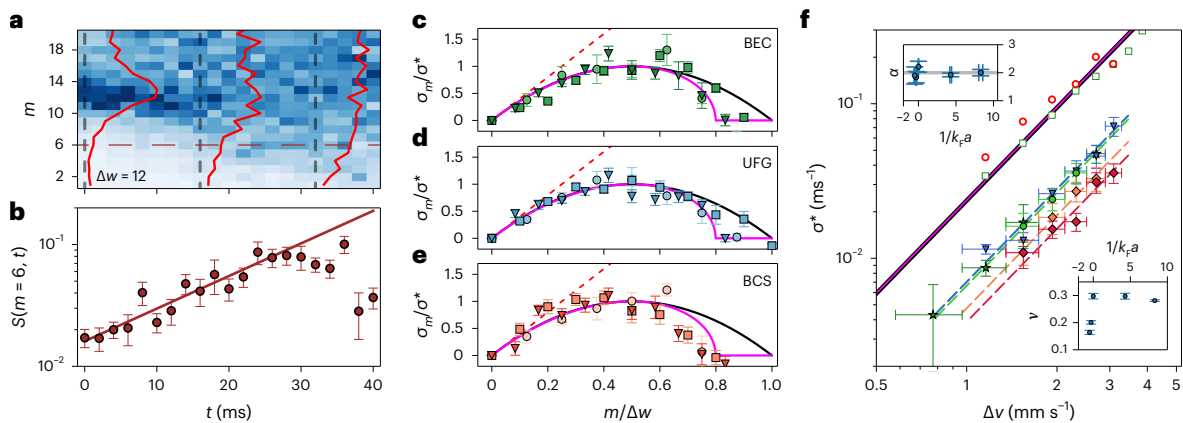

Fig. 3 | Analysis of the vortex array instability across the BCS–BEC crossover.
a, The normalized angular structure factor $s(m, t)$ for a UFG superfluid and $\Delta w = 12$. $s(m, t)$ is extracted by averaging over ~20 experimental realizations. Solid red lines represent vertical cuts $s(m)$, corresponding to angular spectra at different times, and the dashed horizontal line indicates the expected most unstable mode. **b**, Time evolution of s for the most unstable mode, $m^* = 6$. An exponential fit of the data (line) is used to extract the growth rate σ^*. Error bars denote the standard error of the mean over ~20 experimental realizations. **c–e**, Normalized dispersion relations, σ_m/σ^*, as a function of $m/\Delta w$ for the following: BEC ($1/k_F a = 4.3(1)$) (**c**), UFG ($1/k_F a = 0.0(1)$) (**d**) and BCS ($1/k_F a = -0.3(1)$) superfluids (**e**). Rates are shown for different $\Delta w = 8$ (circles), 10 (squares) and 12 (triangles). The dotted red line shows the low-wavenumber limit, $\frac{1}{2}k\Delta v$, normalized to σ^*_{PVM}, while solid lines show the rates predicted by the PVM in

equation (1) (black line) and by Rayleigh's equation (3) using $\delta = 0.8\hbar/M\Delta v$ (magenta line) (see Supplementary Information for the determination of δ). **f**, The scaling of σ^* against Δv in different interaction regimes. Filled symbols correspond to BCS ($1/k_F a = -0.5(1)$, red diamonds; $1/k_F a = -0.3(1)$, orange diamonds), UFG ($1/k_F a = 0.0(1)$, blue triangles) and BEC ($1/k_F a = 4.3(1)$, dark-green stars; $1/k_F a = 8.3(3)$, light-green circles). Open symbols refer to GP simulations at $T = 0$ (open green squares) and cZNG simulations at $T/T_c = 0.4$ (open red circles) for $1/k_F a = 4.3(1)$. Error bars are smaller than the symbols. Solid lines refer to Rayleigh's (magenta) and PVM's (black) predictions. Dashed lines denote fits with $\sigma^* = A\Delta v^\alpha$. Top inset: fitted scaling exponents α as a function of $1/k_F a$. Bottom inset: the adimensional factor ν defined by $\sigma^* = \nu \sigma^*_{PVM}$. In **c–f**, vertical error bars denote fitting 1σ errors while horizontal ones reflect the experimental uncertainty on the initial vortex number.

$$\sigma_{PVM}(k, \Delta v) = \frac{\Gamma k}{2d_v}\left(1 - \frac{kd_v}{2\pi}\right), \quad (1)$$

where $\Gamma = h/M$ is the quantized vortex circulation and $d_v = h/(M\Delta v)$ is the initial inter-vortex separation. The maximum growth rate, σ^*, that

is, the growth rate of the most unstable mode, is reached for $k^* = \pi/d_v$, in agreement with the numerical results reported in ref. 25, where the instability of a linear array of vortices in a single-component BEC is characterized by solving the corresponding Bogoliubov problem. This particular wavenumber sets a fundamental scaling law, $\sigma^* \propto \Delta v^2$,

providing an experimentally accessible hallmark of the instability. In the low-wavenumber limit, $kd_v \ll 1$, equation (1) reduces to $\sigma_{PVM} \sim \frac{1}{2}k\Delta v$, which equals Kelvin's growth rate of a continuous vortex sheet[1] (that is, a zero-width interface). Hence, the PVM extends the classical KHI scenario to the case of a discrete vortex sheet formed by a finite number of vortices. It also predicts a smooth change of the tangential flow between the two layers, except at the position of the vortices, resulting in a finite-size shear layer with half-width $\delta = \hbar/(M\Delta v)$ (Fig. 1b and Supplementary Information).

In our regime of shear velocities, the instability rates have been found to follow the Rayleigh model for the KHI of a finite-width classical shear layer[25]. Although here we extract the rates from the vortex trajectories and not directly from Bogoliubov excitations, we find it interesting to compare our data with the predictions of this classical model (Methods).

In Fig. 3c–e, we show the normalized dispersion relations σ_m/σ^* as a function of $m/\Delta w$ measured for BEC, UFG and BCS superfluids. All the normalized rates are in good agreement with the expected trends from the PVM (equation (1)) and Rayleigh (equation (3) in Methods) formulas. The agreement is more evident for $k \lesssim k^*$, where the rates predicted by the two models are nearly identical, suggesting a close relationship between the instability of the vortex necklace and that of the associated shear flow[25]. In Fig. 3f, the extracted σ^* for different superfluid regimes is plotted as a function of the relative velocity, displaying the expected quadratic behaviour. These scaling properties, together with the normalized dispersion relations in Fig. 3c–e, suggest an interpretation of the dynamics as a quantized analogue of the Kelvin–Helmholtz scenario across the BEC–BCS crossover.

The data in Fig. 3f are compared with equations (1) and (3), and with three-dimensional numerical simulations based on Gross–Pitaevskii (GP) equation and collisionless Zaremba–Nikuni–Griffin (cZNG) model[34]. While theoretical rates—analytical and numerical—agree quantitatively with each other, the measured ones show systematically lower values, quantified by the ratio $v = \sigma^*/\sigma^*_{PVM}$. In classical fluids, dissipation effects (for example, surface tension and viscosity) typically stabilize the system, leading to lower growth rates[1,5,35,36]. In our system, we expect finite temperature to introduce additional dissipative effects through the mutual friction between the superfluid and the non-vanishing normal components. The microscopic origin of this source of dissipation resides in scattering processes between normal excitations and vortices, hence strongly depend on the vortex core structure[37,38]. For instance, in the fermionic regimes, the presence of Andreev quasiparticles localized in the vortex core gives rise to additional dissipation channels[38,39] that should become less relevant moving towards the BEC regime[40]. These effects can be phenomenologically encapsulated in the PVM via the mutual friction coefficients α and α' (Methods). As a result, a partial decrease in the growth rate could be attributed to $\alpha' > 0$. In an attempt to take into account temperature effects at the microscopic level, we have performed numerical simulations of the dynamics using the cZNG model, which includes thermal–condensate interactions only at a mean-field level. As shown in Fig. 3f, the obtained rates are comparable with those from $T = 0$ GP simulations. This approach does not account for the slower rates observed in the experiment. A more complete[34,41] or alternate microscopic model[42,43] should be used to include further effects of the normal component on vortex dynamics. We remark that a quantitative understanding of the microscopic mechanisms connecting non-local vortex dynamics to dissipation, especially in the presence of strong correlations, remains an open problem both experimentally and theoretically[37,38,42]. In addition, we cannot exclude that technical imperfections such as spurious excitations originating from the barrier removal and a non-ideal imprinting procedure (not considered in any of the performed numerical simulations) (Supplementary Information and ref. 29) may potentially foster additional dissipation. Finally, we would like to stress that—essentially due only to quantization of the vorticity
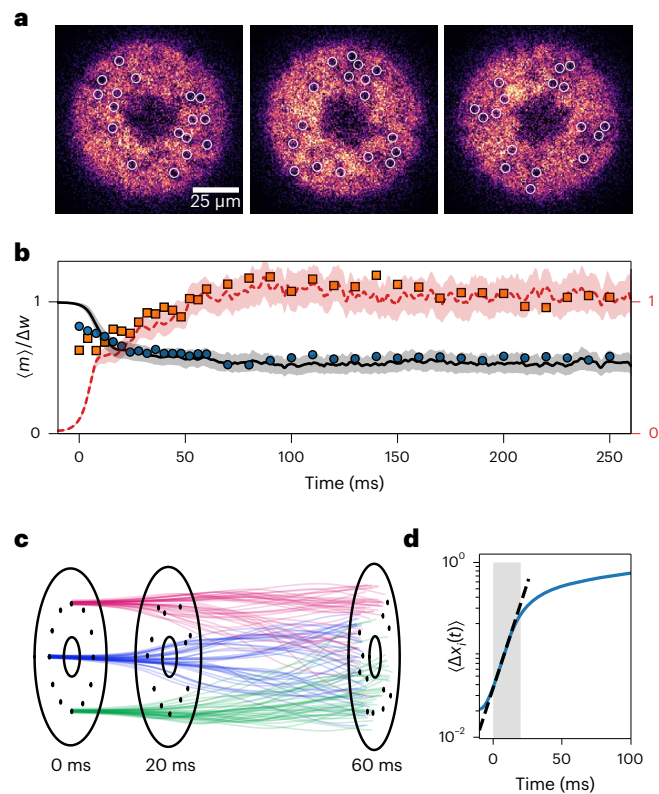
Fig. 4 | Nonlinear vortex dynamics. a, Single-shot TOF images of vortex patterns acquired after 36 ms of evolution, showing twofold, threefold and fourfold vortex cluster symmetries. Images are acquired for a BEC superfluid starting from nominally identical necklaces with $N = 16$. **b**, Time evolution of the mean winding number $\langle m \rangle$ (circles) and its variance $\langle \Delta m^2 \rangle$ (squares) normalized to Δw for $1/k_F a = 4.3(1)$ and $\Delta w = 12$, averaged over ~20 experimental realizations. The data are compared with PVM simulations (solid black and dashed red lines; the shaded region denotes the standard deviation of the mean from 40 realizations). **c**, Trajectories of three vortices (coloured lines) belonging to nearly identical necklaces with $N = 12$. A set of 40 initial vortex positions are picked randomly, each within a range of one healing length $\xi \approx 0.5\,\mu$m around its reference value, for which the necklace is perfectly periodic. We show the vortex pattern at $t = 0$, 20 and 60 ms for one realization. **d**, Mean distance between each vortex trajectory calculated as a function of time by averaging over 40 nearly identical random initial conditions, as described above, and over $N_v = 12$ vortices. The distances are normalized to the mean separation of any given two points in the ring geometry (Methods). At short times, $t < 20$ ms (shaded area), the separation between trajectories grows exponentially (dashed line) with a characteristic maximal Lyapunov exponent of $\Lambda = 0.111(5)\,\text{ms}^{-1}$, in agreement with the maximum instability growth rate $\sigma^*_{PVM} = 0.127(5)\,\text{ms}^{-1}$ obtained for $\Delta w = 12$. Shaded regions around lines denote the standard deviation of the mean.

in units of Γ—the maximum growth rate of the instability takes the universal form $\sigma^* \propto (\Delta v)^2/\Gamma$, irrespective of the considered pairing regime across the BCS–BEC crossover. Interestingly, the proportionality constant, that is, $\pi/4 \times v$, is of order 1 in all regimes.

After the initial stage of the instability, with characteristic time $1/\sigma^*$, the vortex dynamics enter a nonlinear regime with vortex clusters forming and fragmenting as time progresses while conserving the total vortex number. Starting from nominally identical initial conditions, vortices form clusters with different symmetries, as shown in Fig. 4a. Which of these symmetries appears at a given time hinges on the initial conditions and fluctuations in the system. Averaging over different realizations, we observe the system exploring widely different configurations, losing information about the initial order. In particular, the mean winding number $\langle m \rangle$ is nearly constant in time around $\Delta w/2$, while the variance $\langle \Delta m^2 \rangle$ saturates to the vortex number Δw (Fig. 4b).

This indicates that the system reaches a steady state, where all modes are equally populated. PVM simulations starting with nearly identical configurations reproduce the experimental data quantitatively, suggesting that vortices tend to spread over the whole system volume (Fig. 4c).

Signals of the instability are encoded even at the single-vortex level. We compare the vortex trajectories of the different PVM simulations starting from nearby initial conditions and compute their relative separation as a function of time (Fig. 4c,d and Methods). The average separation between same-vortex trajectories grows exponentially, $\sim e^{\Lambda t}$, with a rate Λ similar to the maximal growth rate, σ^*_{PVM} (Fig. 4d). While σ^* quantifies the collective motion of the necklace, the divergence rate Λ — known as the maximal Lyapunov exponent[44] — refers to the trajectory of a single vortex. A positive Λ is here indicative of divergent vortex trajectories starting from arbitrarily close initial conditions of the necklace, and not of chaotic dynamics. This connection clarifies the role of quantized vortices in defining a shear layer and the associated instability as the mechanism behind the breakdown of the vortex necklace. For $t \gg 1/\Lambda$, the distance between trajectories tends to saturate to the average separation of two random points in the system (set by the value 1 in the graph). This is due to the finite-size effects that constrain the trajectory divergence, eventually leading to the attainment of boundary-dominated dynamical equilibrium. On the other hand, such equilibrium hides complex underlying dynamics. Chaotic advection and turbulent flows are expected[45] for point-vortex systems for $N_v > 2$. Classically, shear-flow instabilities such as the KHI in inviscid fluids drive the system into a turbulent state portrayed by an irregular — sensitive to initial conditions — mixing of spiralling structures at different scales[9]. The intertwined vortex trajectories shown in Fig. 4c are reminiscent of this scenario.

Our observation of a shear flow instability in atomic superfluids showcases a pristine example of an emergent phenomenon, with quantized vortices acting simultaneously as sources and probes of the unstable flow. The same microscopic mechanism operates in all superfluid regimes, and it underlies the observed common behaviour, which belongs to the class of classical inviscid fluids with finite-size shear layers. Our work ushers in the exploration of the fundamental connections between quantized vortex dynamics in scalar single-component superfluids and classical shear flow instabilities, posing interesting questions on how the limit of a continuous vortex sheet may be reached within a discretized point-vortex scenario. We anticipate our results to be of relevance for diverse non-equilibrium phenomena in strongly correlated quantum matter, ranging from rapidly rotating quantum gases[23] to pulsar glitches[46] and neutron star mergers[47]. Our findings also set the starting point to explore a variety of vortex matter phase transitions in fermionic superfluids[48], including negative temperature and non-trivial cluster states[49–52]. Moreover, they open prospects for studying the problem of dissipative mechanisms resulting from vortex–quasiparticle interactions in fermionic superfluids[37–39,53]. An exciting direction for future experiments concerns the cascade of secondary instabilities towards the spontaneous onset of quantum turbulence[22,24,54,55], exploring a route complementary to external forcing[56–58] to probe its underlying microscopic mechanisms from the few- to the many-vortex perspective.

Online content

Any methods, additional references, Nature Portfolio reporting summaries, source data, extended data, supplementary information, acknowledgements, peer review information; details of author contributions and competing interests; and statements of data and code availability are available at https://doi.org/10.1038/s41567-024-02466-4.

References

1. Charru, F. *Hydrodynamic Instabilities* (Cambridge Univ. Press, 2011).
2. von Helmholtz, H. Über discontinuierliche Flüssigkeits-Bewegungen [On the discontinuous movements of fluids]. *Monats. Königl. Preuss. Akad. Wiss. Berlin* **23**, 215–227 (1868).
3. Thomson, W. XLVI. Hydrokinetic solutions and observations. *Lond. Edinb. Dubl. Philos. Mag. J. Sci.* **42**, 362–377 (1871).
4. Rayleigh, L. On the stability, or instability, of certain fluid motions. *Proc. London Math. Soc.* **s1-11**, 57–72 (1879).
5. Drazin, P. G. & Reid, W. H. *Hydrodynamic Stability* 1–31 (Cambridge Univ. Press, 2004).
6. Klaassen, G. P. & Peltier, W. R. The onset of turbulence in finite-amplitude Kelvin–Helmholtz billows. *J. Fluid Mech.* **155**, 1–35 (1985).
7. Mashayek, A. & Peltier, W. R. The 'zoo' of secondary instabilities precursory to stratified shear flow transition. Part 2 The influence of stratification. *J. Fluid Mech.* **708**, 45–70 (2012).
8. Thorpe, S. A. Transitional phenomena and the development of turbulence in stratified fluids: a review. *J. Geophys. Res.* **92**, 5231–5248 (1987).
9. Thorpe, S. A. On the Kelvin–Helmholtz route to turbulence. *J. Fluid Mech.* **708**, 1–4 (2012).
10. Reynolds, O. XXIX. An experimental investigation of the circumstances which determine whether the motion of water shall be direct or sinuous, and of the law of resistance in parallel channels. *Philos. Trans. R. Soc. Lond.* **174**, 935–982 (1883).
11. Thorpe, S. A. A method of producing a shear flow in a stratified fluid. *J. Fluid Mech.* **32**, 693–704 (1968).
12. Kent, G. I. Transverse Kelvin–Helmholtz instability in a rotating plasma. *Phys. Fluids* **12**, 2140–2151 (1969).
13. Shearer, E. & Früh, W.-G. Kelvin–Helmholtz instability in a continuously forced shear flow. *Phys. Chem. Earth B* **24**, 487–492 (1999).
14. Bennemann, K.-H. & Ketterson, J. B. *Novel Superfluids* Vol. 2 (Oxford Univ. Press, 2014).
15. Korshunov, S. E. Analog of Kelvin–Helmholtz instability on a free surface of a superfluid liquid. *J. Exp. Theor. Phys.* **75**, 423–425 (2002).
16. Volovik, G. E. On the Kelvin–Helmholtz instability in superfluids. *J. Exp. Theor. Phys.* **75**, 418–422 (2002).
17. Takeuchi, H., Suzuki, N., Kasamatsu, K., Saito, H. & Tsubota, M. Quantum Kelvin–Helmholtz instability in phase-separated two-component Bose–Einstein condensates. *Phys. Rev. B* **81**, 094517 (2010).
18. Suzuki, N., Takeuchi, H., Kasamatsu, K., Tsubota, M. & Saito, H. Crossover between Kelvin–Helmholtz and counter-superflow instabilities in two-component Bose–Einstein condensates. *Phys. Rev. A* **82**, 063604 (2010).
19. Lundh, E. & Martikainen, J.-P. Kelvin–Helmholtz instability in two-component Bose gases on a lattice. *Phys. Rev. A* **85**, 023628 (2012).
20. Kokubo, H., Kasamatsu, K. & Takeuchi, H. Pattern formation of quantum Kelvin–Helmholtz instability in binary superfluids. *Phys. Rev. A* **104**, 023312 (2021).
21. Blaauwgeers, R. et al. Shear flow and Kelvin–Helmholtz instability in superfluids. *Phys. Rev. Lett.* **89**, 155301 (2002).
22. Finne, A. P. et al. Dynamics of vortices and interfaces in superfluid ³He. *Rep. Progr. Phys.* **69**, 3157–3230 (2006).
23. Mukherjee, B. et al. Crystallization of bosonic quantum Hall states in a rotating quantum gas. *Nature* **601**, 58–62 (2022).
24. Baggaley, A. W. & Parker, N. G. Kelvin–Helmholtz instability in a single-component atomic superfluid. *Phys. Rev. A* **97**, 053608 (2018).
25. Giacomelli, L. & Carusotto, I. Interplay of Kelvin–Helmholtz and superradiant instabilities of an array of quantized vortices in a two-dimensional Bose–Einstein condensate. *SciPost Phys.* **14**, 025 (2023).

26. Aref, H. On the equilibrium and stability of a row of point vortices. *J. Fluid Mech.* **290**, 167–181 (1995).

27. Havelock, T. LII. The stability of motion of rectilinear vortices in ring formation. *Lond. Edinb. Dubl. Philos. Mag. J. Sci.* **11**, 617–633 (1931).

28. Kwon, W. J. et al. Sound emission and annihilations in a programmable quantum vortex collider. *Nature* **600**, 64–69 (2021).

29. Del Pace, G. et al. Imprinting persistent currents in tunable fermionic rings. *Phys. Rev. X* **12**, 041037 (2022).

30. Eckel, S., Jendrzejewski, F., Kumar, A., Lobb, C. J. & Campbell, G. K. Interferometric measurement of the current-phase relationship of a superfluid weak link. *Phys. Rev. X* **4**, 031052 (2014).

31. Kanai, T., Guo, W. & Tsubota, M. Merging of rotating Bose–Einstein condensates. *J. Low. Temp. Phys.* **195**, 37 (2019).

32. Thorpe, S. A. The axial coherence of Kelvin–Helmholtz billows. *Q. J. R. Meteorol. Soc.* **128**, 1529–1542 (2002).

33. Warren, B. E. *X-Ray Diffraction* 206–210 (Dover, 1990).

34. Griffin, A., Nikuni, T. & Zaremba, E. *Bose-Condensed Gases at Finite Temperatures* (Cambridge Univ. Press, 2009).

35. Villermaux, E. On the role of viscosity in shear instabilities. *Phys. Fluids* **10**, 368–373 (1998).

36. Betchov, R. & Szewczyk, A. Stability of a shear layer between parallel streams. *Phys. Fluids* **6**, 1391–1396 (1963).

37. Kopnin, N. B. Vortex dynamics and mutual friction in superconductors and Fermi superfluids. *Rep. Progr. Phys.* **65**, 1633 (2002).

38. Sonin, E. B. *Dynamics of Quantised Vortices in Superfluids* 43–77; 213–267 (Cambridge Univ. Press, 2015).

39. Silaev, M. A. Universal mechanism of dissipation in Fermi superfluids at ultralow temperatures. *Phys. Rev. Lett.* **108**, 045303 (2012).

40. Barresi, A., Boulet, A., Magierski, P. & Wlazłowski, G. Dissipative dynamics of quantum vortices in fermionic superfluid. *Phys. Rev. Lett.* **130**, 043001 (2023).

41. Allen, A. J., Zaremba, E., Barenghi, C. F. & Proukakis, N. P. Observable vortex properties in finite-temperature bose gases. *Phys. Rev. A* **87**, 013630 (2013).

42. Mehdi, Z., Hope, J. J., Szigeti, S. S. & Bradley, A. S. Mutual friction and diffusion of two-dimensional quantum vortices. *Phys. Rev. Res.* **5**, 013184 (2023).

43. Sergeev, Y. A. Mutual friction in bosonic superfluids: a review. *J. Low Temp. Phys.* https://doi.org/10.1007/s10909-023-02972-4 (2023).

44. Pikovsky, A. & Politi, A. *Lyapunov Exponents* (Cambridge Univ. Press, 2016).

45. Babiano, A., Boffetta, G., Provenzale, A. & Vulpiani, A. Chaotic advection in point vortex models and two-dimensional turbulence. *Phys. Fluids* **6**, 2465 (1994).

46. Haskell, B. & Melatos, A. Models of pulsar glitches. *Int. J. Mod. Phys. D* **24**, 1530008 (2015).

47. Price, D. J. & Rosswog, S. Producing ultrastrong magnetic fields in neutron star mergers. *Science* **312**, 719 (2006).

48. Sachkou, Y. P. et al. Coherent vortex dynamics in a strongly interacting superfluid on a silicon chip. *Science* **366**, 1480–1485 (2019).

49. Simula, T., Davis, M. J. & Helmerson, K. Emergence of order from turbulence in an isolated planar superfluid. *Phys. Rev. Lett.* **113**, 165302–165302-5 (2014).

50. Johnstone, S. P. et al. Evolution of large-scale flow from turbulence in a two-dimensional superfluid. *Science* **364**, 1267 (2019).

51. Gauthier, G. et al. Giant vortex clusters in a two-dimensional quantum fluid. *Science* **364**, 1264–1267 (2019).

52. Reeves, M. T. et al. Turbulent relaxation to equilibrium in a two-dimensional quantum vortex gas. *Phys. Rev. X* **12**, 011031–011031-18 (2022).

53. Heyl, M. et al. Vortex dynamics in the two-dimensional BCS–BEC crossover. *Nat. Commun.* **13**, 6986 (2022).

54. Kobyakov, D., Bezett, A., Lundh, E., Marklund, M. & Bychkov, V. Turbulence in binary Bose–Einstein condensates generated by highly nonlinear Rayleigh–Taylor and Kelvin–Helmholtz instabilities. *Phys. Rev. A* **89**, 013631 (2014).

55. Barenghi, C. F., Skrbek, L. & Sreenivasan, K. R. Introduction to quantum turbulence. *Proc. Natl Acad. Sci. USA.* **111**, 4647 (2014).

56. Henn, E. A. L., Seman, J. A., Roati, G., Magalh aes, K. M. F. & Bagnato, V. S. Emergence of turbulence in an oscillating Bose–Einstein condensate. *Phys. Rev. Lett.* **103**, 045301–045301-4 (2009).

57. Navon, N., Gaunt, A. L., Smith, R. P. & Hadzibabic, Z. Emergence of a turbulent cascade in a quantum gas. *Nature* **539**, 72–75 (2016).

58. Neely, T. W. et al. Characteristics of two-dimensional quantum turbulence in a compressible superfluid. *Phys. Rev. Lett.* **111**, 235301 (2013).

Methods

Sample preparation

We prepare fermionic superfluid samples by evaporating a balanced mixture of the two lowest hyperfine spin states $|F, m_F\rangle = |1/2, \pm1/2\rangle$ of ^{6}Li, near their scattering Feshbach resonance at 832 G in an elongated, elliptic optical dipole trap formed by horizontally crossing two infra-red beams at a 14° angle. At the end of the evaporation, we sweep the magnetic field to the desired interaction regime. A repulsive TEM_{01}-like optical potential at 532 nm with a short waist of about 13 μm is then adiabatically ramped up before the end of the evaporation to provide strong vertical confinement, $\omega_z \approx 2\pi \times 400$ Hz. Successively, a box-like potential is turned on to trap the resulting sample in a circular region of the x–y plane. This circular box is tailored using a digital micromirror device (DMD). When both potentials have reached their final configuration, the infra-red lasers forming the crossed dipole trap are adiabatically extinguished, completing the transfer into the final uniform pancake trap[28]. Finally, to create the pair of superfluid rings at rest, we dynamically change the DMD-tailored potential. We first create the hole at the centre of the initial disk and then dynamically increase its size until reaching a radius of $R_i = 10.0 \pm 0.2$ μm. Finally, an optical barrier separating the two superfluid rings is adiabatically raised at $R_0 = 27.5 \pm 0.2$ μm. A residual radial harmonic potential of 2.5 Hz is present due to the combined effect of an anti-confinement provided by the TEM_{01} laser beam in the horizontal plane and the confining curvature of the magnetic field used to tune the Feshbach resonance. This weak confinement has a negligible effect on the sample over the $R_e = 45.0 \pm 0.2$ μm radius of our box trap, resulting in an essentially homogeneous density.

Phase-imprinting procedure

We excite controllable persistent current states in each of the two rings by using the phase-imprinting protocol described in ref. 29. Using the DMD, we create an optical gradient along the azimuthal direction, namely $U(r, \theta) = U_0\theta/2\pi \times \text{sign}(r - R_0)$. By projecting such a potential over a time $t_I < \hbar/\mu$, we imprint a phase $\phi(r, \theta) = U(r, \theta) t_I/\hbar$ onto the superfluid wavefunction. By suitably tuning the imprinting time t_I and the gradient intensity U_0, we excite well-defined winding number states in each of the two rings in a reproducible way. We measure the imprinted circulations using an interferometric probe: we let the two rings expand for 3 ms of TOF and then image the resulting spiral-shaped interference pattern. The left panel of Fig. 2b shows an interferogram for $\Delta w = 8$. In particular, the number of spirals in the interferogram yields the relative winding number Δw between the two rings[29,30]. Additionally, we independently check that before the imprinting procedure, the inner ring is in the $w = 0$ state by realizing a similar experimental protocol now in a geometry similar to that reported in ref. 29. All circulation states excited in the two rings have been observed to persist for several hundreds of milliseconds[29], except for $\Delta w > 12$ in the BCS regimes. Nevertheless, we observe these states to not decay for the typical timescale of the observed instability $t < 40$ ms. To reduce the effect of extra density excitation on the dynamics, we wait for 300 ms after imprinting before removing the barrier between the superfluids.

Vortex imaging and tracking

We establish a shear flow by removing the circular barrier separating the two ring superfluids. In particular, we lower its intensity by opportunely changing the DMD pattern. The barrier removal process takes 28 ms and brings the system into the vortex necklace configuration of Fig. 2. We confirm that the duration of the barrier removal does not affect the dynamics. Removing the barrier over time scales faster than 10 ms creates unwanted excitations such as solitonic structures. To image the vortices in the BEC regime, we acquire the TOF image of the superfluid density, where vortices appear as clear holes. In particular, we abruptly switch off the vertical confinement and, at the same time, start to ramp down the DMD potential, removing it completely in 1 ms. Then, we

let the system evolve further for 2.2 ms of TOF and then acquire the absorption image. This modified TOF method allows for the maximization of the vortex visibility. However, the small condensed fraction in the strongly interacting regime makes it impossible to detect vortices with this simple method. Therefore, in the UFG and BCS regimes, we employ the technique developed in ref. 28: we add a linear magnetic field ramp of 4–5 ms to 700 G before the imaging to map the system in a BEC superfluid. The position of the vortices is tracked manually in each acquired image. The size of the vortex limits the error on the position of the vortex after the TOF sequence. To estimate it, we perform a Gaussian fit of the vortex density hole and obtain a waist of ~1.0–1.4 μm for all interaction regimes.

Quasi-2D vortex dynamics

The vertical confinement provided by the $TEM_{1,0}$ laser beam is such that the ratio $\mu/(\hbar\omega_z) \gtrsim 1.5$ in the BEC regimes and $E_F/(\hbar\omega_z) \approx 6$ in the UFG and BCS regimes, making the system collisionally three dimensional. However, vortex dynamics behave as a quasi-2D system since only a few Kelvin modes can be populated. In fact, the standard Kelvin dispersion[38] is

$$\omega(k) = -\frac{\hbar k^2}{2M} \log(\xi k), \qquad (2)$$

where ξ is the healing length. Due to geometrical restrictions[38], only modes with wavelength larger than the healing length can be effectively populated in a superfluid. Under our experimental condition, this translates into the fact that only the lowest wavenumber Kelvin mode with $k = \pi/R_z$ can be populated in the BEC regime, where $R_z = \sqrt{2\mu/(M\omega_z^2)}$ is the Thomas–Fermi radius in the z direction. On the other hand, in the UFG and BCS regimes, due to higher Thomas–Fermi radius and smaller healing length, only the first three Kelvin modes with $k_n = (\pi + 2\pi n)/R_z$ can be populated. Anyway, in all the interaction regimes explored in this work, the number of possibly populated Kelvin modes remains so small that we can assume a 2D dynamics of the vortex motion.

Preparation of the vortex necklace

We remove the circular barrier (Fig. 2a) between the two rings by lowering its intensity using a sequence of 15 different DMD patterns. To obtain a clear initial condition of the vortex crystal and to prevent the formation of other excitation in the system[31], we set the duration of the barrier removal to $\tau = 28$ ms.

After the complete barrier removal, we observe the creation of a vortex necklace with a number of vortices given by the relative circulation Δw, as illustrated in Fig. 2a. The phase imprinting method allows to excite circulation states in the two superfluids in a highly reproducible way, but experimental imperfections can lead to shot-to-shot fluctuations in the circulation state of the rings. This leads to fluctuations in the initial configuration of vortices, which we estimate by analysing the statistics of the relative circulation and vortex number in datasets of 100 experimental realizations on a BEC superfluid at $1/k_F a_s = 4.1(1)$. Extended Data Fig. 1a shows the distribution of the measured relative circulation between the two rings $\langle\Delta w\rangle_M$ with respect to the target Δw_T, measured from interferograms acquired before removing the circular barrier for $\Delta w_T = 6$ and $\Delta w_T = 12$. In Extended Data Fig. 1b, the number of spurious vortices introduced by the phase-imprinting protocol is displayed, measured from the TOF expansion of the two rings before the barrier removal. Finally, Extended Data Fig. 1c shows the distribution of the total number of vortices in the superfluid detected in the TOF expansion after removing the circular barrier. Despite the high reliability in producing the desired circulation states in the two rings (Extended Data Fig. 1a), we observe that the distribution of the total number of vortices detected after the barrier removal is augmented and broadened by the presence of spurious vortices. This leads to

residual fluctuations of the initial configurations of the vortex necklace (Extended Data Fig. 1d), which determine the experimental uncertainty on the initial relative velocity Δv (Fig. 3f,g, horizontal error bars). They also contribute to the experimental noise on the extracted exponential growth rate for a given Δw.

Rayleigh model

In classical fluid mechanics, the problem of the stability of a finite-width shear layer was first analysed by Rayleigh[4], who derived an interface-dependent growth rate as

$$\sigma_R(k, \Delta v) = \mathrm{Im} \frac{\Delta v}{4\delta} \sqrt{(2k\delta - 1)^2 - e^{-4k\delta}}. \tag{3}$$

Here, δ is the interface width and depends on the fluid's specifics and the flow shear velocity. According to equation (3), the instability only occurs for $k\delta \le 0.64$, while the system is stable against perturbations with higher wavenumbers[1]. Similar to the PVM, equation (3) recovers Kelvin's rate for $k\delta \ll 1$.

PVM

We consider a 2D superfluid containing N point vortices with quantized circulations $\Gamma = h/M$. When the inter-vortex separation is greater than a few healing lengths, vortices are advected by the velocity field created by other vortices. The equation of motion of each vortex is $d\mathbf{r}_i/dt = \mathbf{v}_i^0$, where $\mathbf{v}_i^0$ is the velocity field created by all the other vortices. If we consider a one-dimensional array of equispaced vortices at coordinates $(x_n, y_n) = (d_v/2 + nd_v, 0)$, moving in a 2D space of coordinates (x, y) without boundaries, the tangential velocity of the superfluid flow can be written as

$$v_x(x, y) = -\frac{\Gamma}{2d_v} \frac{\sinh(2\pi y/d_v)}{\cosh(2\pi y/d_v) + \cos(2\pi x/d_v)}. \tag{4}$$

From this relation, the width of the shear layer is naturally expressed in units of $\delta = d_v/(2\pi)$, or equivalently $\delta = \hbar/(M\Delta v)$.

When considering the ring geometry, $\mathbf{v}_i^0$ must take into account the boundary conditions, namely that the flow must have a zero radial component at both the internal (R_i) and external (R_e) radii. We include the boundary conditions by using the method of image vortices (Supplementary Information) and solve the equation of motions for the vortex necklace configuration in the ring with the Runge–Kutta method of fourth order. From the obtained trajectories of the vortices, $\mathbf{r}_i(t)$, we compute the normalized angular structure factor $s(m, t)$.

Let us remark that vortices arranged in a ring array are not necessarily unstable, as noted by Havelock[27]. When the vortex array encloses an inner boundary without circulation, the array is unstable only for $N \ge 7$. Moreover, finite vortex number heavily suppresses the growth rate, converging to equation (1) for $N \gg 100$. On the other hand, when the array encloses the inner boundary having a circulation $w_i = N/2$, the array is unstable for $N \ge 2$. In the latter setup, the growth rate converges to equation (1) already for $N \ge 6$, justifying its application in the present work (Supplementary Information).

Dissipative effects in the PVM

The effect of dissipation on vortex dynamics can be introduced in the context of the two-fluid model as the effect induced by the mutual friction within the normal and superfluid components. This model, coined the dissipative PVM, includes two mutual friction coefficients α and α' associated with a dissipative term and a reactive term, respectively. Assuming that the normal component is at rest, meaning, $v_n = 0$, the dissipative PVM describes the motion of the vortices, $\frac{d\mathbf{r}_i}{dt} = (1 - \alpha')\mathbf{v}_i^0 - \alpha\kappa_i\hat{z} \times \mathbf{v}_i^0$, where $\kappa_i = \pm 1$ is the vortex sign with respect to the

vertical z-axis. This modification introduces the correction factor $|\gamma_d| = \sqrt{(1 - \alpha')^2 + \alpha^2}$ into the growth rate given by equation (1) (Supplementary Information). It is worth remarking that $|\gamma_d|$ can be either larger or smaller than 1, depending of the specific values of the mutual friction coefficients.

Angular structure factor analysis

At $t = 0$, the one-dimensional angular structure factor of a finite array of N_v vortices placed in a perfect necklace arrangement, with angular coordinates $\theta_j^0 = 2\pi j/N$, is $S^0(m) = \sin^2(\pi m)/(N_v \sin^2(\pi m/N_v))$. The departure from the necklace configuration can be modelled through the small fluctuations in the vortex positions at $t = 0$: $\theta_j = \theta_j^0 + \delta\theta$. In crystals, small fluctuations ($\delta\theta \ll 2\pi/N_v$) are considered as a disorder of the first kind[33] and they modify the structure factor as $S(m, t) \approx S^d(m) - m^2\langle\delta\theta^2\rangle(t)S^d(m)$, where $S^d(m)$ corresponds to the structure factor of a given realization, and in general, $S^d(m) \ne 0$ for different m. In the limit case, taking the average over many realizations, $S^d(m) \to S^0(m)$. Here, the temporal dependence of $S(m, t)$ is entirely provided by the term $\langle\delta\theta^2\rangle(t)$. In the context of the PVM[26,27], the motion of the vortices is linked to the underlying shear flow instability. In particular, the deviation from their initial position grows as $\delta\theta \sim e^{\sigma_m t}$, where σ_m is given by equation (1). Therefore, the temporal evolution of the structure factor is $S(m, t) \sim e^{2\sigma_m t}$.

Maximum growth rate σ*

To obtain the maximum growth rate σ^* experimentally, we fit the dispersion relation of the measured rates (Fig. 2c–e) using the function $f(x, \sigma^*) = \sigma^* \frac{\sqrt{e^{-4\eta x} - (2\eta x - 1)^2}}{A}$, with $x = m/\Delta w$ and $A = \max\left[\sqrt{e^{-4\eta x} - (2\eta x - 1)^2}\right] = (W(e^{-1}) + 1)/(2\eta) \approx 0.639/\eta$, where $W(x)$ is the Lambert W function and $\eta = 0.8$ (see Supplementary Information for details). The function $f(x, 1)$ corresponds to equation (3) normalized to the maximum value shown as the magenta line in Fig. 2c–e. We perform the fit of the dispersion relation letting σ^* as the only free parameter.

Lyapunov exponent

To extract the Lyapunov exponent, Λ, of the system, we perform 40 PVM simulations under nearly identical conditions for a necklace with $N = 12$. The initial positions of each vortex are taken randomly within a range of one healing length (0.5 μm) around their reference values for a perfectly periodic necklace. We then define the function $\mathcal{L}_k = \langle|\mathbf{r}_i^k - \mathbf{r}_j^k|\rangle_{i,j}$ as the average distance between two simulated trajectories of the kth vortex in the necklace. Here, we denote by $\langle\cdot\rangle_{i,j}$ the average over different simulations, that is, $i, j = 0, ..., 40$. Then, we compute the average over the N vortices $\langle\Delta\mathbf{x}\rangle = \langle\mathcal{L}_k\rangle_k$, which we report in Fig. 4d after normalizing it to the mean separation of any two points in the ring geometry $\bar{d} = \int_\Omega \int_\Omega \sqrt{(x - x')^2 + (y - y')^2}\, dx\, dy\, dx'\, dy'/A^2$, where Ω is the ring region with area $A = \pi(R_e^2 - R_i^2)$. Although $\bar{d}$ is straightforward to write, computing the integrals to obtain an analytical result is quite involved. For this reason, we numerically evaluate it by taking 10^5 random points uniformly distributed inside the ring geometry delimited by R_i and R_e. Then, we compute the 10^{10} possible combinations for the point-to-point distances and calculate their average value to estimate the mean separation $\bar{d} \approx 41.78 \pm 0.02$ μm. We extract the characteristic rate Λ from a fit of the initial trend in $\langle\Delta\mathbf{x}\rangle$ over the first 14 ms from the starting time of the instability.

Data availability

The data that support the figures within this paper are available from the corresponding author upon reasonable request. Source data are provided with this paper.

Author contributions

D.H.-R., G.D.P., F.S., F.M. and G.R. conceived the study. D.H.-R., N.G., G.D.P. and W.J.K. performed the experiments. D.H.-R. and N.G. analysed the experimental data. D.H.-R., K.X., C.F. and M.M. carried out numerical simulations. All authors contributed to the interpretation of the results and to the writing of the manuscript.

Competing interests

The authors declare no competing interests.

Additional information

Extended data is available for this paper at https://doi.org/10.1038/s41567-024-02466-4.

Supplementary information The online version contains supplementary material available at https://doi.org/10.1038/s41567-024-02466-4.

Correspondence and requests for materials should be addressed to D. Hernández-Rajkov.

Peer review information *Nature Physics* thanks the anonymous reviewers for their contribution to the peer review of this work.

Reprints and permissions information is available at www.nature.com/reprints.
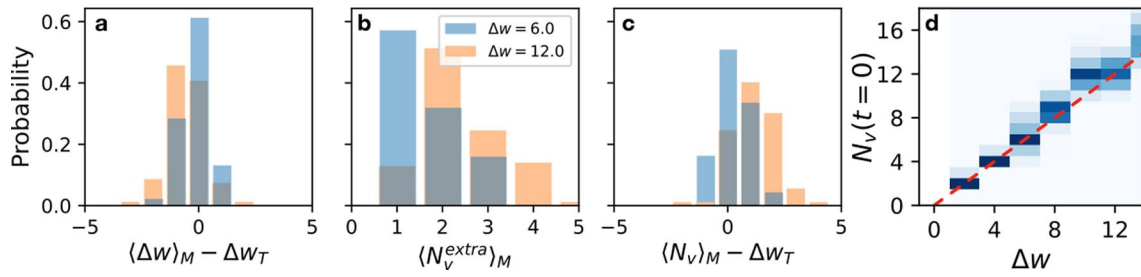
Extended Data Fig. 1 | Reproducibility of the initial cloud preparation.
a, Fidelity in creating the target circulation state state, $\langle \Delta w \rangle_M - \Delta w_T$. **b**, Number of
spurious vortices observed before removing the optical barrier, and **c**, Deviation
of the total number of vortices from the target state, $\langle N_v \rangle_M - \Delta w_T$. All three
panels were generated from 100 experimental repetitions for each of the two
target states $\Delta w_T = 6, 12$ (blue and orange, respectively). **d**, Total number of
vortices detected after removing the barrier, $t = 0$ of vortex dynamics, as a
function of the imprinted winding number difference Δw_T. The red dashed line
is the identity line, $N_v = \Delta w$.